

LaminoDiff: Artifact-Free Computed Laminography in Non-Destructive Testing via Diffusion Model

Tan Liu, Liu Shi, Binghuang Peng, Tong Jia, Xiaoling Xu, Baodong Liu, and Qiegen Liu, *Senior Member, IEEE*

Abstract—Computed Laminography (CL) is a key non-destructive testing technology for the visualization of internal structures in large planar objects. The inherent scanning geometry of CL inevitably results in inter-layer aliasing artifacts, limiting its practical application, particularly in electronic component inspection. While deep learning (DL) provides a powerful paradigm for artifact removal, its effectiveness is often limited by the domain gap between synthetic data and real-world data. In this work, we present LaminoDiff, a framework to integrate a diffusion model with a high-fidelity prior representation to bridge the domain gap in CL imaging. This prior, generated via a dual-modal CT-CL fusion strategy, is integrated into the proposed network as a conditional constraint. This integration ensures high-precision preservation of circuit structures and geometric fidelity while suppressing artifacts. Extensive experiments on both simulated and real PCB datasets demonstrate that LaminoDiff achieves high-fidelity reconstruction with competitive performance in artifact suppression and detail recovery. More importantly, the results facilitate reliable automated defect recognition.

Index Terms—computed laminography, aliasing artifact, circuit packaging inspection, diffusion model.

I. INTRODUCTION

COMPUTED Laminography (CL) has emerged as a premier non-destructive testing (NDT) modality, particularly indispensable for the inspection of large-scale planar components such as high-frequency printed circuit boards (PCBs) and semiconductor wafers [1]–[4]. Fig. 1 compares the scanning geometries of CT and CL. Unlike Computed Tomography (CT) [5], which mandates a scanning trajectory perpendicular to the rotation axis as shown in Fig. 1(a), CL employs an inclined geometry described in Fig. 1(c). This configuration effectively circumvents the limitation of excessive X-ray attenuation paths inherent in planar objects, granting access to projection angles geometrically unreachable by CT. However,

This work was supported by the National Natural Science Foundation of China (Grant: 621220033 and 62201193), Nanchang University Youth Talent Training Innovation Fund Project (Grant: XX202506030012), Early-Stage Young Scientific and Technological Talent Training Foundation of Jiangxi Province (Grant: K1202509220191) and by data from the Institute of High Energy Physics, Chinese Academy of Sciences, Beijing, China.

T. Liu and L. Shi are co-first authors. Corresponding authors: B. Liu and Q. Liu.

T. Liu, B. Peng, L. Shi, X. Xu and Q. Liu are with the School of Information Engineering, Nanchang University, Nanchang 330031, China (e-mail: {liutan, BH_Peng}@email.ncu.edu.cn; {shiliu, xuxiaoling, liuqiegen}@ncu.edu.cn).

T. Jia and B. Liu are with the Beijing Engineering Research Center of Radiographic Techniques and Equipment, Institute of High Energy Physics, Chinese Academy of Sciences, Beijing 100049, China; are also with the School of Nuclear Science and Technology, University of Chinese Academy of Sciences, Beijing 100049, China; and the Jinan Laboratory of Applied Nuclear Science, Jinan 250100, China (e-mail: {jiatong, liubd}@ihep.ac.cn).

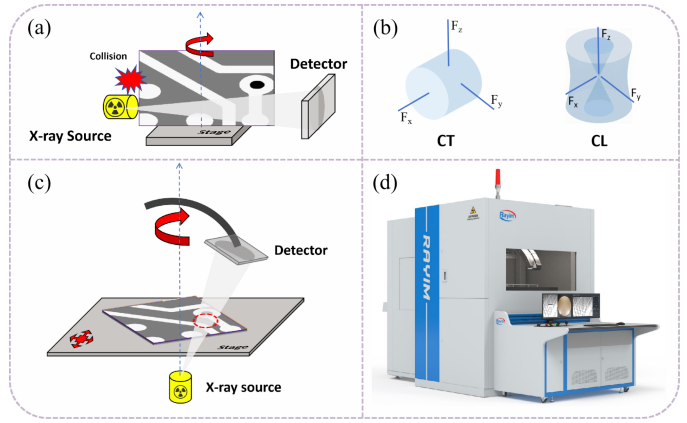


Fig. 1. Scanning geometry of CT and CL. (a) CT geometry with orthogonal rotation. (b) A schematic diagram of the spectrum in the Fourier domain. (c) CL geometry featuring an inclined rotation axis. (d) The commercial CL inspection system at the Institute of High Energy Physics, Chinese Academy of Sciences (Beijing).

image reconstruction in this setup is fundamentally an ill-posed inverse problem constrained by the missing cone and the violation of Tuy-Smith data completeness conditions [6], [7]. Fig. 1(b) visually exemplifies this objective degradation pattern inherent to the laminographic geometry. While the analytical FDK algorithm [8] is widely adopted for its efficiency [9], it suffers from incompleteness [10]. Although various improvements—such as truncation correction [11], inter-layer deblurring [12], [13], and virtual re-projection [14]—have been proposed, severe aliasing artifacts and z -axis blurring remain intrinsic.

To further suppress noise and artifacts, iterative algorithms based on variational principles have become mainstream [15]. These approaches typically focus on designing regularizers tailored to CL imaging features, such as handling anisotropy via structure tensors [16], [17], adapting gradient sparsity [18], [19], or decoupling z -axis smoothing from in-plane preservation [20]. Additionally, specific solvers have been developed for large-scale local scanning tasks [21]. Despite their effectiveness, the high computational cost and sensitivity to hyperparameter tuning limit industrial scalability. Besides, leveraging external priors or CT-CL fusion offers an alternative strategy to recover high-quality information. Existing strategies include fusing CT completeness with CL resolution [22], utilizing the generalized Fourier slice theorem for frequency filling [23], [24], or exploiting defect-free reference priors [25]. Nevertheless, these explicit fusion methods necessitate high-precision registration, which necessitates complex param-

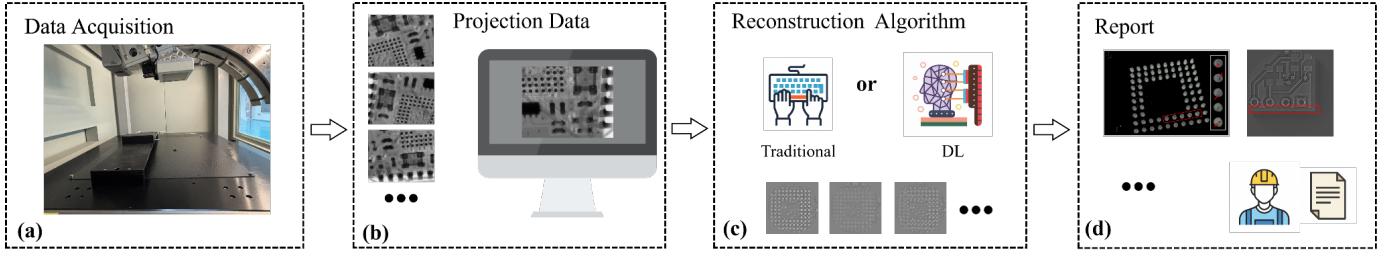


Fig. 2. Workflow of the CL-based inspection system. The process typically involves (a) data acquisition using the CL system, (b) projection data collection, (c) image reconstruction, and (d) final defect detection and reporting.

eter tuning, and the fusion reconstruction is highly sensitive to parameters.

In recent years, deep learning has revolutionized tomographic imaging [26], [27], yet its adaptation to laminography imaging remains fraught with challenges. Pioneering works have utilized Convolutional Neural Networks (CNNs) for tasks such as motion artifact correction [28], automated metrology, segmentation [29]–[31], and microdefects detection [32], [33]. Nevertheless, deterministic regression models face a fundamental physical paradox: the scarcity of ground truth labels. Obtaining an artifact-free reference for physical CL data is practically intractable due to the missing cone. Consequently, establishing a high-fidelity paired dataset is the primary prerequisite for effective model learning.

To construct reliable supervision targets, prior works have explored unsupervised domain adaptation techniques, such as CycleGAN [34], to synthesize pseudo-labels. While effective in aligning textural distributions, these adversarial methods often struggle to preserve the strict structural fidelity required for precision inspection, potentially introducing structural inconsistencies or hallucinations [35]. To avoid these uncertainties, we introduce a physics-informed supervision strategy that diverges from purely data-driven paradigms. We employ the CT-CL fusion reconstruction to construct high-fidelity data. By integrating this fusion result directly as a rigorous training target, our strategy effectively injects physical consistency into the deep learning pipeline, establishing a robust label.

Notably, the iterative refinement mechanism of the diffusion model [36]–[38] demonstrates remarkable effectiveness in solving complex inverse imaging problems, especially in finite-angle CT scenarios [39], [40]. Inspired by these works, we propose a diffusion-based framework to learn the complex degradation distribution from synthetic data, thereby achieving robust generalization to real-world experimental acquisitions.

In order to realize this objective, we propose a novel framework termed **LaminoDiff**, shortening the domain gap with the fusion strategy based on diffusion model. Distinct from deterministic regression models that are prone to overfitting specific simulation textures, LaminoDiff reformulates CL reconstruction as a prior-constrained conditional generative process. The core of the architecture is the incorporation of a latent-space fusion prior, which guides the data reconstruction process to maintain structural consistency. This structural constraint enables the network to focus exclusively on iteratively restoring fine-grained textures and high-frequency details typically obscured by aliasing. By effectively disentangling structural recovery from the artifact reduction task, our model bridges the synthesis-to-reality gap, facilitating the robust generalization of learned degradation patterns to complex real-world scenarios.

The main contributions of this work are summarized as follows:

- We propose LaminoDiff, a guided diffusion framework to recover high-fidelity structural details from aliased observations. This method guides the reconstruction by introducing priors, reformulating the reconstruction problem as a generative process with structural constraints. This approach effectively ensures structural consistency and mitigates complex aliasing, overcoming the limitations of deterministic regression models in detail recovery.
- We propose a physical prior generation strategy based on dual-scale CT-CL fusion. To address the domain gap issue, we utilize high-fidelity fusion reconstruction as a rigorous training objective. Unlike pseudo-labels, this strategy introduces physical consistency into the process and establishes a robust benchmark for artifact reduction.
- Experiments on both simulated and real datasets validated the LaminoDiff's effectiveness in removing artifacts. Furthermore, the recovery of internal microstructures demonstrated the framework's practical value in high-precision nondestructive testing.

The rest of this paper is organized as follows: Section II briefly reviews relevant research. Section III elaborates on the theoretical framework and delves into our proposed method. Section IV presents comparative experimental results. Finally, Section V discusses the proposed method and provides concluding remarks.

II. RELATED WORKS

A. CL Reconstruction

CL reconstruction is an inverse problem modeling X-ray interactions. Letting $x \in \mathbb{R}^N$ be the object and $y \in \mathbb{R}^M$ be the measurements, the linear system is defined as:

$$y = \mathcal{A}x + \eta, \quad (1)$$

where \mathcal{A} is the CL system matrix and η denotes noise. Analytically, the FDK algorithm approximates the solution as follows:

$$x_{fdk} = \mathcal{B}(\mathcal{H} * (\mathcal{W} \cdot y)), \quad (2)$$

where \mathcal{W} , \mathcal{H} , and \mathcal{B} represent the geometry correction weight, filter, and the back-projection operator, respectively. To mitigate missing cone artifacts inherent in analytical methods, iterative reconstruction incorporates prior knowledge by optimizing:

$$x^* = \arg \min_x \left[\frac{1}{2} \|y - \mathcal{A}x\|_2^2 + \lambda \mathcal{R}(x) \right], \quad (3)$$

where the first term enforces data fidelity, $\mathcal{R}(x)$ imposes priors, λ governs the strength of prior constraint. While iterative methods improve quality, they are computationally expensive. Consequently, deterministic regression models approximate the inverse mapping \mathcal{N}_θ by minimizing the loss:

$$\theta^* = \arg \min_\theta \sum_i \|\mathcal{N}_\theta(x_{input}^{(i)}) - x_{label}^{(i)}\|^2, \quad (4)$$

where inputs are initial reconstructions. However, supervised learning in CL is constrained by the physical intractability of obtaining artifact-free targets.

B. Diffusion Models

Diffusion models are generative frameworks that learn data distributions through forward noise addition and reverse denoising. Denoising Diffusion Probabilistic Models (DDPM) model the forward process as a Markov chain [37]. Through the property of Gaussian distributions, the distribution of the state x_t at any timestep t given x_0 can be explicitly expressed as:

$$q(x_t|x_0) = \mathcal{N}(x_t; \sqrt{\bar{\alpha}_t}x_0, (1 - \bar{\alpha}_t)\mathbf{I}), \quad (5)$$

where $\bar{\alpha}_t = \prod_{s=1}^t (1 - \beta_s)$ denotes the cumulative product of the signal schedule, determined by the variance schedule β_s . Unlike GANs, the learning objective simplifies to matching the noise distribution via a parameterized network ϵ_θ .

The reverse process approximates the intractable posterior $q(x_{t-1}|x_t)$ using a learned Gaussian transition $p_\theta(x_{t-1}|x_t) = \mathcal{N}(x_{t-1}; \mu_\theta, \Sigma_\theta)$. The distribution mean μ_θ is typically parameterized by predicting the added noise ϵ_θ , formulated as:

$$\mu_\theta(x_t, t) = \frac{1}{\sqrt{\bar{\alpha}_t}} \left(x_t - \frac{1 - \bar{\alpha}_t}{\sqrt{1 - \bar{\alpha}_t}} \epsilon_\theta(x_t, t) \right). \quad (6)$$

While standard DDPMs require iterating through this stochastic chain, Denoising Diffusion Implicit Models (DDIM) [38] introduce a non-Markovian generalization that permits deterministic sampling, significantly accelerating inference.

For conditional tasks aiming to sample from a target distribution $p(x|c)$, where c denotes the conditioning signal, classifier-free guidance [41] has become the de facto standard for balancing fidelity and diversity. Instead of training auxiliary classifiers, it modifies the score estimate by extrapolating between a conditional model $\epsilon_\theta(x_t|c)$ and an unconditional counterpart $\epsilon_\theta(x_t)$. The guided noise prediction $\tilde{\epsilon}_\theta$ is formulated as:

$$\tilde{\epsilon}_\theta = (1 + w) \cdot \epsilon_\theta(x_t|c) - w \cdot \epsilon_\theta(x_t), \quad (7)$$

where $w > 0$ is a scalar guidance scale. This mechanism effectively steers the generation towards the high-density regions of the conditional distribution $p(x|c)$ without the complexity of external gradients.

III. METHODOLOGY

A. CT-CL Fusion Targets Construction

1) *Fusion Framework*: In deep learning-based CL reconstruction, establishing a physically consistent supervision target is prerequisite to resolving the inverse problem. The CL acquisition process is modeled as $y_{cl} = \mathcal{A}_{cl}x + \eta$. Due to the limited angular range, \mathcal{A}_{cl} possesses a non-trivial null space, leading to a deterministic loss of spectral information in the reconstruction x . In the fourier domain, a deterministic zero-region known as the missing cone can be mathematically expressed as:

$$\mathcal{F}(x)(\omega) \approx 0, \quad \forall \omega \in \Omega_{null}, \quad (8)$$

where \mathcal{F} denotes the fourier transform, ω represents the spatial frequency vector, and Ω_{null} is the spectral region inaccessible to the laminographic geometry.

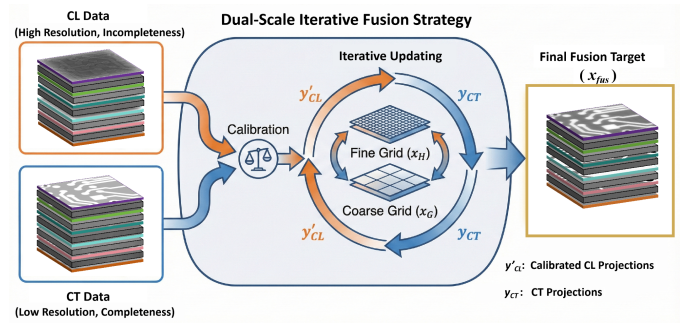


Fig. 3. Schematic of the dual-scale iterative fusion framework. The process begins by calibrating the intensity of the high-resolution CL data with the complete CT data. These inputs are then fed into the iterative fusion strategy. Through an alternating update scheme involving both a coarse grid (x_G) and a fine grid (x_H), the algorithm synergizes the spatial precision of CL with the completeness of CT, yielding a high-fidelity fusion target x_{fus} .

To construct a label x_{label} that is both spatially precise and spectrally complete, we adopt the dual-scale fusion reconstruction algorithm based on OS-SART. The schematic of this proposed framework is illustrated in Fig. 3. Unlike single-modal data augmentation, this approach synergizes the high resolution of CL with the angular completeness of CT. To ensure data consistency before fusion, we establish a linear mapping based on the mean intensity of common sub-regions. Let y_{cl} be the raw CL projections, the calibrated CL projections y'_{cl} are obtained by:

$$y'_{cl} = y_{cl} \times \frac{\text{Mean}(x_{ct})}{\text{Mean}(x_{cl})}, \quad (9)$$

where x_{ct} and x_{cl} represent the reconstructed values of the same sub-region from independent CT and CL scans, respectively.

We defined two voxel grids for fusion iteration: A coarse-grained grid for global object x_G and a fine-grained grid x_H for the target region. The fusion process utilizes an alternating forward and backward projection scheme. In each iteration k , x_H are updated jointly by both y_{ct} and calibrated y'_{cl} to minimize the error in both domains. The update rule for

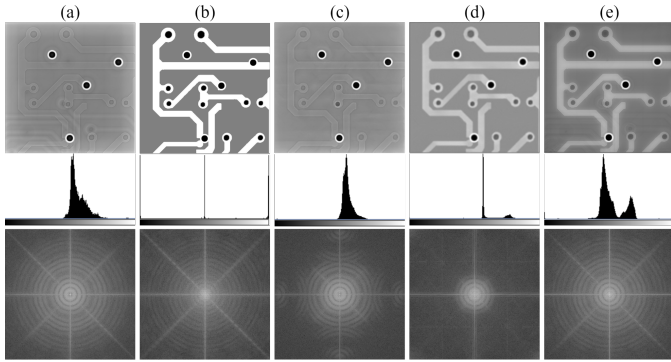


Fig. 4. Comparison of different targets. The figure evaluates the signal features of four label strategies across spatial (top row), histogram (middle row), and spectral (bottom row) domains. (a) The original reconstruction results contain aliasing artifacts. (b) Numerical phantom with statistically binary. (c) The pseudo-labels generated by CycleGAN-CL. (d) The pseudo-labels generated by CycleGAN-CT. (e) The proposed CT-CL fusion label.

the fine-grained grid x_H in the fusion loop is formulated as follows:

$$x_H^{(k+1)} = x_H^{(k)} + \lambda N^{-1} \mathcal{A}^T \left(y_s - \left[\mathcal{A}(x_H^{(k)}) + \mathcal{A}(x_G^{(k)}) \right] \right), \quad (10)$$

where λ denotes the relaxation factor, and N is the diagonal normalization matrix. The term y_s represents the measured projection data for the current subset, which dynamically alternates between y_{cl}' and y_{ct} throughout the iterations. Simultaneously, x_G is updated using a similar back-projection, with operators adapted to the lower resolution. Upon convergence, the optimized x_H , which integrates the high resolution of CL with the missing-cone compensation from CT, is extracted and assigned as the high-fidelity label x_{target} for the subsequent supervised learning tasks.

2) *Fidelity Analysis of Supervision Targets*: Label quality sets a theoretical upper limit on the network's reconstruction capability [42], [43]. We define the relationship between them. Let f_θ denote the neural network parameterized by θ , x_{fdk} the input data, x_{target} the target data, and x_{gt} the ideal label. The ultimate goal is to minimize the discrepancy between the network output and the physical truth. Following the decomposition of generalization error in inverse problems [44], the total error is bounded by:

$$\underbrace{|f_\theta(x_{fdk}) - x_{gt}|}_{\text{Total Reconstruction Error}} \leq \underbrace{|f_\theta(x_{fdk}) - x_{target}|}_{\text{Optimization Error}} + \underbrace{|x_{target} - x_{gt}|}_{\text{Label Bias}}. \quad (11)$$

Eq. (11) reveals that even if the network perfectly optimizes the training loss, the final reconstruction fidelity is strictly limited by the inherent bias of the label $|x_{target} - x_{gt}|$ [45]. Therefore, minimizing this label bias is a prerequisite for high-performance reconstruction. We conducted multidimensional comparative analyses across spatial, spectral, and statistical domains. Fig. 4 comprehensively illustrates the visual and quantitative comparisons of different potential supervised signals. We examined the signal features of each strategy.

Fig. 4(b) exhibits ideal spatial structures with infinitely sharp edges and demonstrates a broadband spectrum with perfect high-frequency coverage. However, the discrete binary

peaks in its histogram lack authentic X-ray physical properties. Consequently, training on such targets results in an excessively large domain gap, leading to network overfitting and the generation of unnatural boundaries.

We analyze a data augmentation strategy based on unpaired image-to-image transformation. Fig. 4(c) aligns the style with CL but fails to correct underlying physical defects. Its Fourier spectrum exhibits a chaotic structure, while the unimodal histogram distribution renders copper lines indistinguishable from the substrate, making it a counterproductive supervisory signal. Similarly, Fig. 4(d) fills the central low-frequency region, providing a clean spatial background. However, the rapid decay of high-frequency components leads to blurred edges and detail loss. Furthermore, the excessively narrow histogram peaks lack the necessary variance for high-precision reconstruction.

Finally, our proposed dual-scale fusion label in Fig. 4(e) exhibits higher fidelity. It fills in missing regions using CT information while preserving the high-frequency spectral support feature of CL. In spatial domain, it can be seen that the image fuses the sharp edge definition of CL and the uniform background of CT. The histogram shows a clear bimodal distribution, and the variance within the signal peaks is consistent with reality. This confirms that, among the compared methods, the fusion label is the supervisory target with the highest physical consistency and spatial accuracy.

B. Iterative Training Strategy

To obtain high-fidelity reconstructions, we utilize the prepared CT-CL fusion data x_{fus} as the target data x_0 for training. This section details the slice-wise input strategy, the network architecture, and the optimization objective.

1) *Spatial Coupling Strategy*: The core is to guided the recovery of fine-grained structural details in the generative process by severe aliasing artifacts. As illustrated in Fig. 5(a), the forward process follows a fixed Markov chain that gradually adds Gaussian noise to the clean fusion label x_0 . For any timestep $t \in [1, T]$, the noisy state x_t can be sampled directly using the reparameterization trick:

$$x_t = \sqrt{\bar{\alpha}_t} x_0 + \sqrt{1 - \bar{\alpha}_t} \epsilon, \quad \epsilon \sim \mathcal{N}(0, \mathbf{I}), \quad (12)$$

where ϵ represents the standard Gaussian noise, and $\bar{\alpha}_t$ follows the schedule defined previously.

In the reverse process, unlike text-to-image models that inject semantic priors via latent cross-attention, our task requires accurate pixel-level alignment to correct the inherent defects in CL images. In order for the network to effectively learn the correlation between the artifact data and the target data, we propose a direct spatial coupling strategy. We construct a unified input tensor $x_{in} \in \mathbb{R}^{(C+2) \times H \times W}$ at each timestep t at each timestep t by explicitly concatenating the noisy state with the condition signals along the channel dimension. x_{in} can be mathematically formulated as:

$$x_{in} = \text{Concat}(x_t, x_{fdk}, x_{fus})_{\text{dim}=\text{channel}}, \quad (13)$$

where x_{fdk} denotes the input data and x_{fus} represents the fusion guidance data which provides explicit structural priors. By

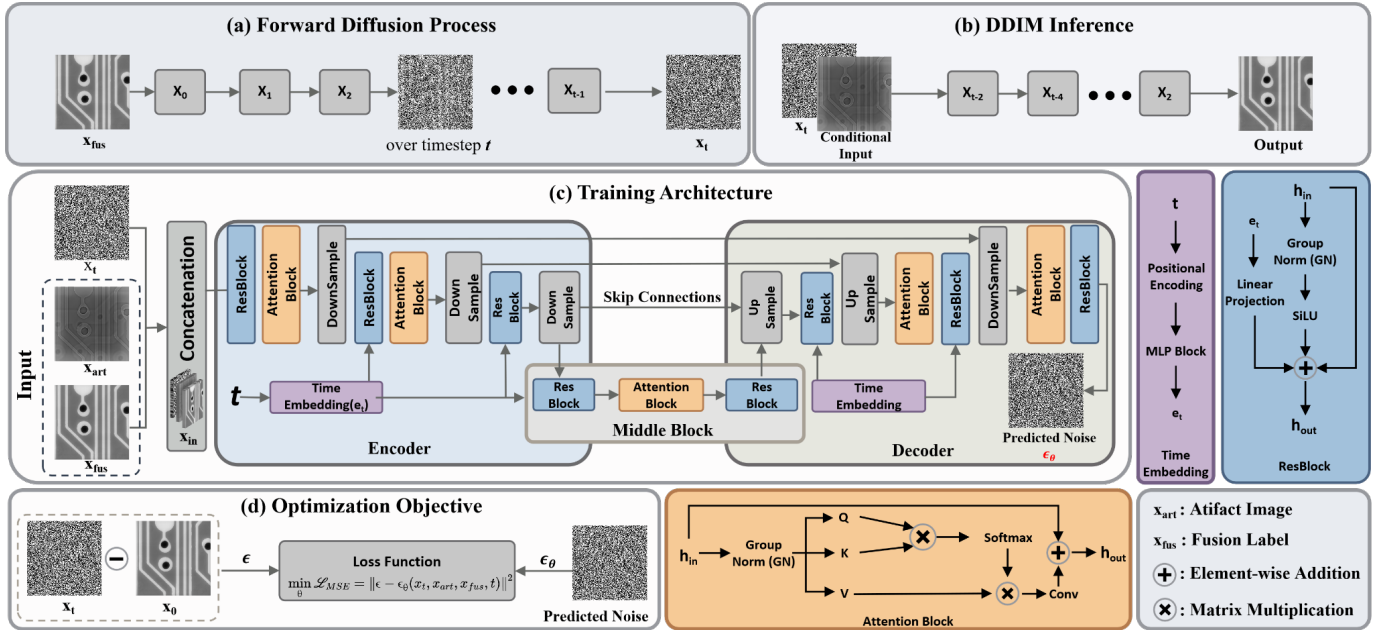


Fig. 5. Schematic illustration of the proposed diffusion-based reconstruction framework. (a) Forward Diffusion Process: Gaussian noise is progressively added to the clean fusion label x_{fus} to generate the noisy state x_t . (b) DDIM Inference: The artifact-free image is iteratively reconstructed from noise via DDIM, conditioned on the CL x_{fdk} . (c) Training Architecture: A U-Net with skip connections processes the concatenated inputs (x_t, x_{fdk}, x_{fus}) using ResBlocks and Attention mechanisms to extract multi-scale features. (d) Optimization Objective: The model is trained to predict the added noise ϵ_θ by minimizing the loss.

stacking these 2D signals in the input, the initial convolutional kernels of the encoder are compelled to learn joint spatial features from the very first layer. This design imposes a strong inductive bias, ensuring that the generated features for x_t are locally anchored to the structural boundaries provided by x_{fus} and the intensity distribution of x_{fdk} , thereby preserving edges often lost in purely attention-based mechanisms.

2) *Network Architecture and Optimization*: The noise prediction network ϵ_θ , illustrated in Fig. 5(c), employs a U-Net-based architecture. To facilitate dynamic denoising across varying noise levels, the scalar timestep t is first mapped to a sinusoidal positional embedding $e_{pos} \in \mathbb{R}^d$, followed by a Multi-Layer Perceptron (MLP) to obtain the time embedding vector e_t :

$$e_t = \text{MLP}(e_{pos}) = \mathbf{W}_2 \cdot \text{SiLU}(\mathbf{W}_1 \cdot e_{pos}), \quad (14)$$

where SiLU is the activation function, and $\mathbf{W}_1, \mathbf{W}_2$ are learnable parameters. This time embedding is injected into residual block to modulate the feature maps. Let \mathbf{h}_{in} be the input feature map of a block, and the output \mathbf{h}_{out} is computed by adding the scale-shift modulated features to the original input:

$$\mathbf{h}_{out} = \mathbf{h}_{in} + \text{Conv}(\text{SiLU}(\text{GN}(\mathbf{h}_{in}))) + \mathbf{W}_{proj} \cdot e_t, \quad (15)$$

where GN denotes group normalization and $\mathbf{W}_{proj} \in \mathbb{R}^{C \times D}$ represents a learnable linear projection matrix. This matrix aligns the dimensionality of the time embedding e_t with the channel dimension of the feature map, allowing the temporal information to be broadcasted and added spatially as a channel-wise bias. Recognizing that aliasing artifacts exhibit a global distribution, we explicitly integrate Spatial

Attention Blocks at lower resolutions. Given an input feature map, the query (Q), key (K), and value (V) matrices are obtained via linear projections using learnable weight matrices $\mathbf{W}_Q, \mathbf{W}_K$, and \mathbf{W}_V , respectively. The attention operation then computes the global dependencies as follows:

$$\text{Attention}(Q, K, V) = \text{softmax} \left(\frac{QK^T}{\sqrt{d_k}} \right) V, \quad (16)$$

where d_k is the scaling factor. This mechanism generates a global attention map QK^T that relates every pixel to every other pixel, enabling the network to distinguish extensive aliasing artifacts from structural components regardless of their spatial distance. Furthermore, long-range skip connections concatenate encoder features with decoder features, preserving fine-grained details essential for identifying micro-circuit defects.

The network ϵ_θ essentially functions as a function approximator for the conditional score $\nabla_{x_t} \log p(x_t | x_{fdk}, x_{fus})$. As described in Fig. 5(d), we adopt a supervised training strategy where the global optimization objective is minimized using the weighted mean squared error (MSE):

$$\mathcal{L} = \mathbb{E}_{x_0, \epsilon, t} \|\epsilon - \epsilon_\theta(x_t, t, x_{fdk}, x_{fus})\|_2^2. \quad (17)$$

Minimizing Eq. (17) drives the network to utilize the explicit structural cues from the fusion prior x_{fus} to rectify the distorted regions in x_{fdk} . This formula anchors the generative trajectory to the correct structural information, ensuring the output x_0 aligns with both the data consistency of the input and the structural fidelity of the fusion target.

C. Iterative Reconstruction via DDIM

During the inference phase, the solution space is traversed solely using pre-trained prior knowledge and the input x_{fdk} in Fig. 5(b). To robustly handle the uncertainty caused by information loss, we employ a deterministic sampling strategy based on a DDIM.

We interpret the trained denoiser ϵ_θ as a conditional score function estimator. This allows us to explicitly approximate the gradient of the log-density of the data distribution given the x_{fdk} as:

$$\nabla_{x_t} \log p_t(x_t | x_{fdk}) \approx -\frac{1}{\sqrt{1-\bar{\alpha}_t}} \epsilon_\theta(x_t, t, x_{fdk}), \quad (18)$$

where $\bar{\alpha}_t$ is the noise schedule parameter, and x_{fdk} encapsulates the necessary data consistency constraints.

To further enforce conformity to the input and prevent the generation of hallucinated structures in blurred regions, we adopt a classifier-free guidance strategy. By intermittently masking the condition x_{fdk} during training, the network learns both conditional and unconditional distributions. During inference, we extrapolate the noise estimate to amplify the influence of the input data, formulating the rectified noise $\hat{\epsilon}_t$ as:

$$\hat{\epsilon}_t = \epsilon_\theta(x_t, t, \emptyset) + s \cdot \underbrace{[\epsilon_\theta(x_t, t, x_{fdk}) - \epsilon_\theta(x_t, t, \emptyset)]}_{\text{Data Consistency}}, \quad (19)$$

where $s \geq 1$ denotes the guidance scale. By decoupling the unconditional noise from the conditional noise, this vector acts as a data-consistency. It suppresses generated features that are plausible but inconsistent with the input x_{fdk} , while explicitly enhances the unique topological boundaries presented in artifacts.

For the inference phase, we employ the deterministic DDIM update rule using the rectified noise $\hat{\epsilon}_t$. The previous state x_{t-1} is computed as:

$$x_{t-1} = \sqrt{\bar{\alpha}_{t-1}} \left(\frac{x_t - \sqrt{1-\bar{\alpha}_t} \cdot \hat{\epsilon}_t}{\sqrt{\bar{\alpha}_t}} \right) + \sqrt{1-\bar{\alpha}_{t-1}} \cdot \hat{\epsilon}_t, \quad (20)$$

where the first term represents the predicted clean image at the current step, strictly constrained by $\hat{\epsilon}_t$ to preserve high-frequency fidelity. The second term defines the deterministic direction pointing to x_t , ensuring the process iteratively removes noise while maintaining the structural layout consistent with the input x_{fdk} . The workflow of LaminoDiff can be represented as Algorithm 1.

IV. EXPERIMENTS

Our framework was implemented using PyTorch on a workstation equipped with a single NVIDIA RTX 5880 Ada GPU (48 GB). The training corpus consisted of 100 synthetic six-layer PCB phantoms, simulated to ensure high diversity in circuit layout and imaging artifacts. We employed the AdamW optimizer with an initial learning rate of 1×10^{-4} . The model was trained for 300,000 iterations with a batch size of 2 to minimize the objective function defined in Eq. (17). To validate the proposed method, we compared it against representative baselines spanning different reconstruction paradigms: the

Algorithm 1 LaminoDiff: Training and Iterative Reconstruction

Representation Learning

Input: Paired dataset $\mathcal{D} = \{x_{fus}, x_{fdk}\}$.

Output: Optimized noise prediction network ϵ_θ .

```

1: repeat
2:   Sample data pair  $(x_{fus}, x_{fdk})$  and timestep  $t \sim \mathcal{U}(1, T)$ .
3:   Sample noise  $\epsilon \sim \mathcal{N}(0, \mathbf{I})$ .
4:    $x_t \leftarrow \sqrt{\bar{\alpha}_t} x_{fus} + \sqrt{1-\bar{\alpha}_t} \epsilon$ 
5:   Take a gradient descent step on:
6:    $\nabla_\theta \|\epsilon - \epsilon_\theta(x_t, t, x_{fdk}, x_{fus})\|^2$ 
7: until converged
8:
Iterative Reconstruction
Input: Artifact observation  $x_{fdk}$ , Trained network  $\epsilon_\theta$ .
Output: Reconstructed image  $x_0$ .
9:  $x_T \sim \mathcal{N}(0, \mathbf{I})$ 
10: for  $t = T, \dots, 1$  do
11:    $\hat{\epsilon}_t \leftarrow \text{Compute Rectified Noise}(x_t, x_{fdk}, \omega)$ 
12:    $\hat{x}_{0|t} \leftarrow (x_t - \sqrt{1-\bar{\alpha}_t} \hat{\epsilon}_t) / \sqrt{\bar{\alpha}_t}$ 
13:    $x_{t-1} \leftarrow \sqrt{\bar{\alpha}_{t-1}} \hat{x}_{0|t} + \sqrt{1-\bar{\alpha}_{t-1}} \cdot \hat{\epsilon}_t$ 
14: end for
15: return  $x_0$ 

```

analytical FDK algorithm, the iterative SART algorithm, a supervised U-Net, and a CycleGAN-based style transfer method. All baselines were optimized under identical experimental conditions to ensure a fair comparison. Code for LaminoDiff is available at <https://github.com/yqx7150/LaminoDiff>.

We employed Peak Signal-to-Noise Ratio (PSNR), Structural Similarity Index Measure (SSIM), Mean Squared Error (MSE) and Correlation Coefficient (CC) for standard image quality assessment [46]. Furthermore, to explicitly quantify geometric fidelity critical for PCB inspection, we introduced the Binary Difference Maps (BDM) metric. BDM assesses structural layout accuracy through a two-step process. First, the reconstructed image I and the ideal phantom P_m are binarized using Otsu's thresholding τ [47]:

$$B(i, j) = \begin{cases} 1, & \text{if } I(i, j) > \tau, \\ 0, & \text{otherwise.} \end{cases} \quad (21)$$

Subsequently, BDM calculates the percentage of pixel-wise agreement between the binary maps:

$$\text{BDM} = \left(1 - \frac{\sum_{i,j} |B_{rec}(i, j) - B_{ph}(i, j)|}{N \times M} \right) \times 100 \quad (22)$$

where $B_{rec}(i, j)$ and $B_{ph}(i, j)$ denote the binary values of the reconstructed image and the reference phantom at pixel coordinate (i, j) , respectively. The term $N \times M$ represents the total pixel count. A higher BDM indicates superior recovery of the underlying circuit geometry.

A. Datasets Preparation

To rigorously evaluate the performance and generalization capability of LaminoDiff, we constructed three distinct test

TABLE I
SCANNING PARAMETERS OF CL SYSTEM

Parameter	Value
Source to Rotation Center	19.32 mm
Focus to Stage	16.35 mm
Focus to Zero Plane	201.63 mm
Radius of Rotation	10.32 mm
Detector unit size	0.0495 mm
Pixel Size	0.005 mm
Tilt Angle	30°
Projection views	360
Exposure time for each projection	1s

datasets ranging from in-distribution simulations to real-world acquisitions. The specific scanning parameters for all datasets are detailed in Table I.

1) *Simulated Homologous Dataset*: To establish a rigorous in-distribution benchmark, we constructed a high-fidelity synthetic dataset emulating complex six-layer high-density interconnect PCB architectures. The dataset comprises 101 distinct numerical phantoms, each generated via a stochastic The structural layout engine that randomizes circuit routing, via placement, and layer stacking to ensure structural diversity. The projection data were synthesized using the exact cone-beam scanning geometry detailed in Table I, incorporating realistic noise modeling to mirror the physics of the CL acquisition process. 100 phantoms constituted the training corpus to learn the manifold of PCB structures, while one distinct phantom was exclusively reserved for testing.

2) *Simulated Heterogeneous Dataset*: To rigorously evaluate the model's generalization capability across topological domain shifts, we constructed a heterogeneous test set, explicitly termed the MPCB dataset. The structural layout of this phantom was reconstructed based on the complex circuit benchmarks established in the study of sequential regularization-based CL [20]. Compared to the stochastic generator used for training, the MPCB phantom exhibits significantly higher wiring density, representing a challenging Out-of-Distribution sample. Despite these architectural discrepancies, the forward projection simulation adhered strictly to the scanning geometry defined in Table I. This experimental design isolates the topological structure as the sole variable, thereby verifying that the model's performance is driven by learned physical priors rather than overfitting to specific training patterns.

3) *Real-World Experimental Dataset*: To validate the practical applicability and domain-transfer capability of LaminoDiff, we conducted real-world data acquisition in collaboration with the Institute of High Energy Physics (IHEP), Chinese Academy of Sciences (Beijing). The physical scanning setup is described in Fig. 6. To ensure a comprehensive evaluation, the acquisition campaign comprised three distinct physical samples. Data were acquired using a commercial industrial Computed Laminography system. The X-ray source was operated at a tube voltage of 80 kV and a target current of 75 μ A. To accommodate the planar geometry of the objects, the tilt angle was fixed at 30°. Crucially, to facilitate a direct evaluation of the method's transition from simulation

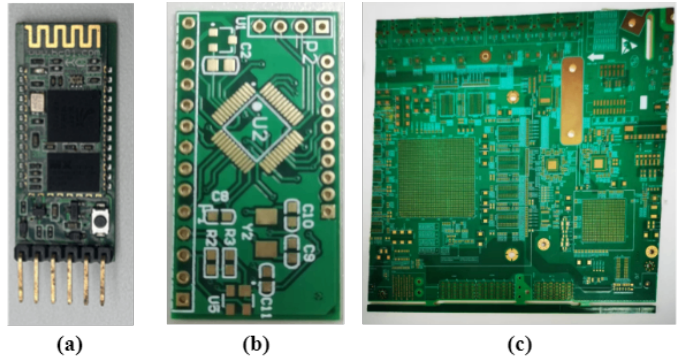


Fig. 6. Optical photograph of the multi-layer PCB samples used for real-world data acquisition. (a) PCB sample used for the cross-sectional evaluation of multilayer circuit boards and the volumetric rendering of BGA solder balls. (b) PCB sample used for the global reconstruction of physical PCB layers. (c) PCB sample used for the structural restoration of high-frequency signal stubs.

to reality, all other geometric configurations—including the source-to-detector distance and magnification factors—were strictly aligned with the simulation settings detailed in Table I. This dataset introduces real-world stochastic variations, such as electronic noise and focal spot blurring, serving as a critical benchmark for the proposed method.

B. Simulated Homologous Study

1) *Qualitative Visual Comparison*: The visual comparison of the reconstructed PCB phantom is presented in Fig. 7. As observed in Fig. 7 (b) and (c), traditional analytical and iterative methods struggle with the limited-angle geometry. The FDK algorithm produces severe artifacts and suffers from low contrast, failing to delineate the fine circuit traces. While SART improves edge definition to some extent, it remains susceptible to pronounced artifacts and noise, particularly evident in the inter-trace regions. Deep learning-based baselines exhibit different types of degradation. The U-Net result effectively suppresses high-frequency noise but introduces uncharacteristic blocky artifacts and intensity inhomogeneity, especially around the high-density vias, leading to structural unfaithfulness. CycleGAN, while enhancing contrast significantly, suffers from geometric distortion and hallucination. It generates pseudo-structures with excessive brightness around the vias, deviating from the ground truth morphology. In contrast, the proposed LaminoDiff demonstrates superior performance in both artifact removal and detail preservation. It successfully reconstructs the sharp edges of the traces without introducing the smoothing effects seen in U-Net or the geometric deformations observed in CycleGAN. These visual improvements are consistently validated by the quantitative metrics in Table II.

2) *Quantitative Intensity Profile Analysis*: To provide a rigorous quantitative assessment of reconstruction fidelity, Fig. 7(g) plots the intensity profiles along the trajectory indicated in Fig. 7(a). An ideal reconstruction should manifest as a rectangular wave, characterized by uniform high intensity within the material, zero intensity in the background, and steep gradients at the structural boundaries. As illustrated in

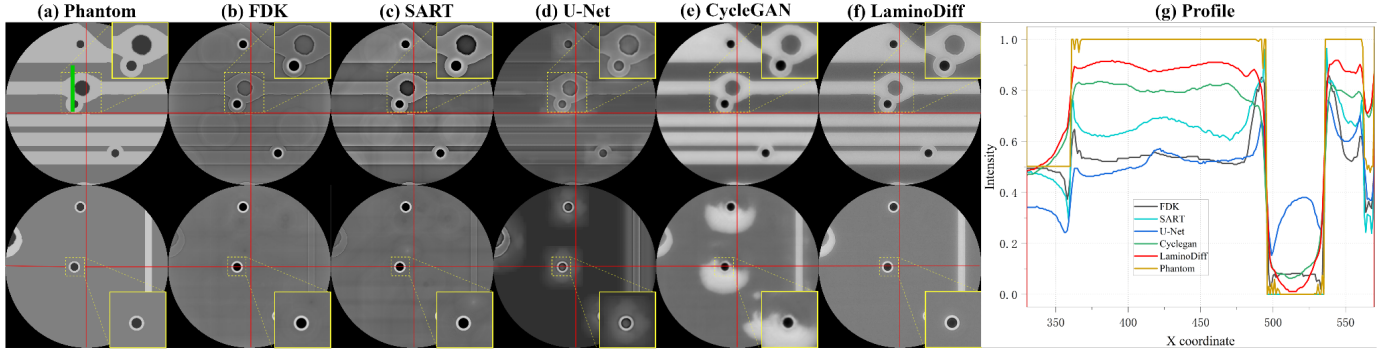


Fig. 7. Qualitative comparison of reconstruction methods on the simulated PCB phantom. (a) Reference, (b) FDK, (c) SART, (d) U-Net, (e) CycleGAN, and (f) LaminoDiff, (g) Quantitative intensity profile analysis of reconstruction results. Row 1: conductive layer(Slice 3); Row 2: conductive layer(Slice 80). All images are displayed with a grayscale window of [25.5, 284.5].

TABLE II
QUANTITATIVE EVALUATIONS OF DIFFERENT METHODS FOR SIMULATED HOMOLOGOUS STUDY

Method	PSNR \uparrow	SSIM \uparrow	MSE \downarrow	BDM \uparrow	CC \uparrow
FDK	13.18	0.8657	0.0560	22.67	0.3247
SART	14.94	0.8064	0.0413	76.17	0.7876
U-Net	9.48	0.7076	0.1237	31.96	0.4069
CycleGAN	18.04	0.8923	0.0157	81.57	0.8217
LaminoDiff	19.58	0.9110	0.0118	93.94	0.8846

TABLE III
QUANTITATIVE EVALUATIONS OF DIFFERENT METHODS FOR SIMULATED HETEROGENEOUS STUDY

Method	PSNR \uparrow	SSIM \uparrow	MSE \downarrow	BDM \uparrow	CC \uparrow
FDK	8.92	0.6769	0.1283	83.86	0.8409
SART	14.69	0.8494	0.0382	80.92	0.8204
U-Net	9.78	0.6671	0.1062	34.14	0.3718
CycleGAN	16.30	0.8595	0.0236	92.53	0.9196
LaminoDiff	18.47	0.9110	0.0159	93.19	0.9600

Fig. 7(g), the analytical FDK and iterative SART methods suffer from severe contrast loss, with intensity values significantly lower than the ground truth. The U-Net results exhibit a critical flaw: it produces erroneous intensity elevations in the void regions, indicating a failure to correctly separate the foreground from the background. While CycleGAN improves the intensity level compared to analytical methods, it still fails to reach the peak density of the phantom and exhibits fluctuations indicative of heterogeneous reconstruction. In contrast, the proposed LaminoDiff demonstrates superior fidelity. First, it achieves the highest contrast recovery, with intensity levels that most closely track the ground truth in both the material and background regions. The flatness of the purple curve within the high-intensity regions confirms that our method effectively suppresses the low-frequency non-uniformities commonly seen in FDK and SART. Second, regarding edge preservation, LaminoDiff exhibits sharp transitions at the material boundaries. The slope of the intensity drop-off is significantly steeper than that of the competing methods, verifying that LaminoDiff effectively mitigates blurring and preserves the geometric accuracy of the circuit traces.

C. Simulated Heterogeneous Study

To assess the robustness of the proposed method against domain shifts, we performed validation on the mPCB dataset. Although this dataset remains within the simulation domain, its structural complexity and conductor density significantly exceed those of the training set, posing a substantial challenge for generalization. As shown in Fig. 8, traditional methods (FDK and SART) exhibit low contrast and severe aliasing

artifacts, causing the fine details of the high-density traces to merge indistinguishably. Deep learning also struggle to generalize to this out-of-distribution data. U-Net tends to amplify edge artifacts and introduces blocky distortions, failing to recover the sharp boundaries of the circuit pads. CycleGAN produces attenuated intensities and hallucinated textures. More critically, in the vertical cross-sectional views, CycleGAN fails to preserve the inter-laminar separation, resulting in a loss of distinct layer information in the z -direction. Conversely, LaminoDiff demonstrates superior generalization performance. It faithfully reconstructs the complete circuitry with high contrast, effectively resolving minute details such as the central apertures, which are blurred in other methods. Furthermore, the vertical cross-section confirms that LaminoDiff maintains structural integrity and clear stratification between layers. These visual improvements are consistently validated by the quantitative metrics in Table III.

D. Real-World Experimental Study

1) *Cross-Sectional Evaluation of Multilayer Circuit Boards:* Fig. 9 illustrates the reconstruction results for two distinct axial layers and their sagittal plane. As observed in Fig. 9(a), the image obtained by the FDK algorithm has extremely low contrast and severe artifacts. The traces are barely distinguishable from the substrate. U-Net tends to over-smooth the image, blurring the edges of the holes and introducing horizontal artifacts in the cross-sectional view. CycleGAN, while attempting to enhance texture, generates noisy results with hallucinated granular layout, failing to provide a clean separation of layers. In contrast, LaminoDiff delivers a remarkable improvement in

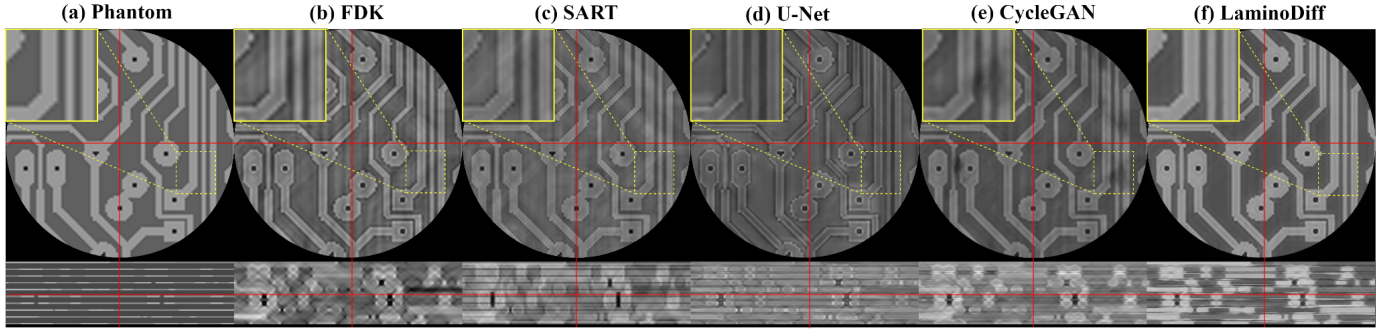


Fig. 8. Qualitative comparison of reconstruction results on the real mPCB dataset. Row 1: Conductive layer slice; Row 2: Z-axis cross-section. All images are displayed with an intensity range of [-40.5, 236.5].

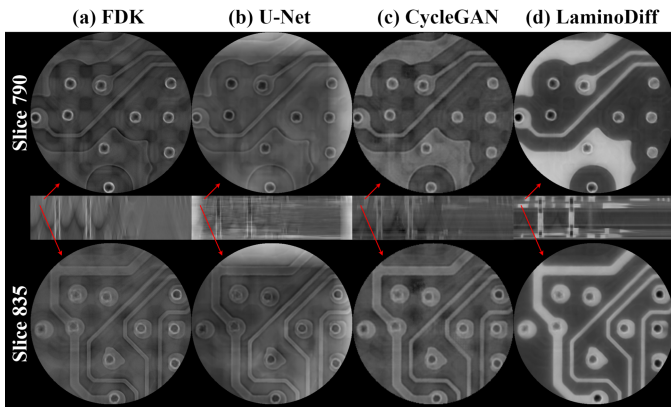


Fig. 9. Qualitative evaluation on real-world CL data acquired from a physical PCB sample. The figure displays reconstruction results from two different axial layers: Slice 790 and Slice 835. All images are displayed with a grayscale window of [62.5, 229.5].

image quality. In the axial views, it effectively suppresses the system noise and restores high contrast, making the circuit structural clearly visible. The boundaries of the pads and traces are sharp and distinct. The sagittal plane demonstrate the method's superior 3D consistency. While other methods produce smeared or discontinuous vertical profiles, LaminoDiff clearly reconstructs the vertical interconnect access—visible as distinct pillar-like structures—and the horizontal stratification of the PCB layers.

2) *Global Reconstruction of Physical PCB Layers:* To verify the scalability of our method for industrial inspection, Fig. 10(e) displays the complete reconstructed layer of the physical PCB, generated by stitching the patch-wise predictions of LaminoDiff. The magnified comparisons of the highlighted ROI are shown in Fig. 10(a)-(d). The FDK result captures the macroscopic layout but is heavily compromised by inherent limitations. Aliasing artifacts at the boundaries of the metallic traces degrade the effective resolution, and the low contrast results in inadequate signal separation between the traces and the substrate. The U-Net method exhibits severe over-smoothing. It fails to preserve high-frequency details, causing the sharp edges of the circuit traces to blur significantly. Consequently, the distinct layout of the circuitry becomes ambiguous. CycleGAN improves sharpness relative

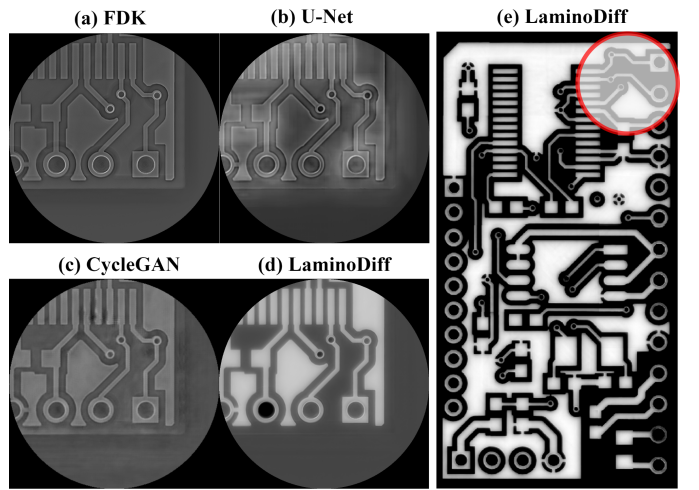


Fig. 10. Reconstruction results on a real-world PCB. (a)-(d) Magnified comparisons of the ROI corresponding to the area marked by the red circle in (e). The full field-of-view reconstruction of the entire circuit layer, obtained by stitching the local patches processed by the proposed LaminoDiff. All images are displayed with a grayscale window of [62.5, 229.5].

to U-Net but introduces non-structural artifacts. Notably, distinct dark patches and intensity inhomogeneities appear near the boundaries of the board, which can be misinterpreted as material defects. In contrast, the proposed LaminoDiff achieves the best visual fidelity in both local and global contexts. Locally, it produces a clean background with a minimal noise floor and renders the circuit edges with high acuity. Fine features, such as the precise circular contours of the holes and the thin connection lines, are reconstructed without the blurring seen in U-Net or the artifacts observed in FDK. Globally, the stitched full-field image demonstrates excellent spatial consistency. The method maintains uniform contrast across the entire board, confirming that LaminoDiff is robust enough to handle data reconstruction tasks effectively.

3) *Volumetric Rendering of BGA Solder Balls:* To further validate the practical applicability of our method in industrial NDT, we performed 3D volume rendering on a BGA-packaged chip. The geometric integrity of solder balls and the detection of internal voids are critical quality control metrics in electronics manufacturing. As illustrated in Fig. 11, the FDK reconstruction captures the general array layout but

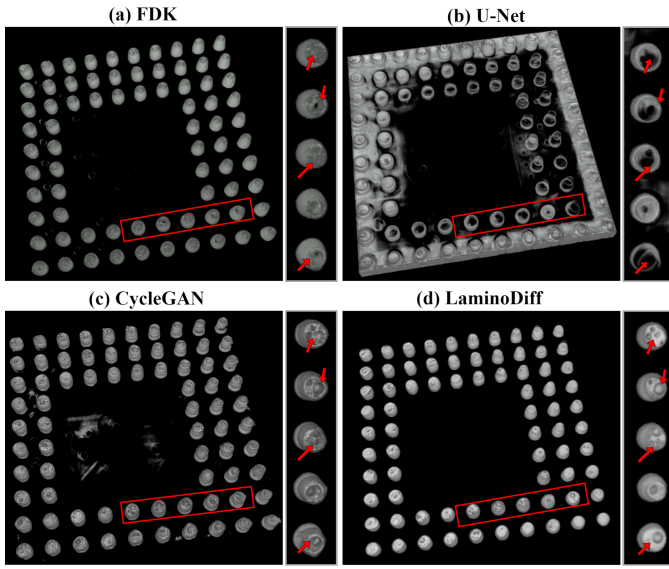


Fig. 11. 3D volume rendering evaluation on a real-world BGA chip. Each subfigure displays the overall 3D isometric view, a magnified ROI of individual solder balls. The red arrows indicate internal voids within the solder balls.

is heavily degraded. The solder balls appear elongated in the vertical cross-section, and the surfaces are plagued by granular noise. Although some low-density regions are vaguely visible, the boundaries are too ill-defined for accurate defect characterization. U-Net fails to resolve individual solder balls, producing a cloud-like conglomeration with severe artifacts that obscure the entire BGA array. The vertical profile is completely distorted. CycleGAN achieves better separation than U-Net but introduces excessive particle noise on the ball surfaces and suffers from inter-layer aliasing in the central region, making it difficult to distinguish true defects from hallucinated noise. In sharp contrast, LaminoDiff yields a reconstruction of superior quality. It accurately recovers the 3D morphology of each solder ball. The magnified ROIs demonstrate the method's exceptional capability in resolving internal details. The internal voids are clearly delineated with sharp boundaries against the clean, noise-free solder material. On a global scale, the solder balls are distinctly separated without the artifacts seen in U-Net. This high-fidelity reconstruction provides a reliable data foundation for downstream tasks.

4) Structural Restoration of High-Frequency Signal Stubs: To demonstrate the restoration of geometric fidelity essential for precise analysis, we examined a critical microstructure—the stub—in a high-frequency PCB. In high-speed signal transmission, the physical length of stubs is a decisive factor affecting signal integrity; therefore, dimensional quantification is paramount for industrial quality control. As illustrated in Fig. 12, the FDK reconstruction is heavily compromised by severe inter-layer aliasing artifacts. The resulting surface appears fuzzy, creating significant geometric ambiguity. In such a degraded state, defining the exact termination points of the stub is virtually impossible, rendering reliable automated measurement infeasible. Conversely, LaminoDiff successfully suppresses these artifacts, recovering a clean, solid 3D struc-

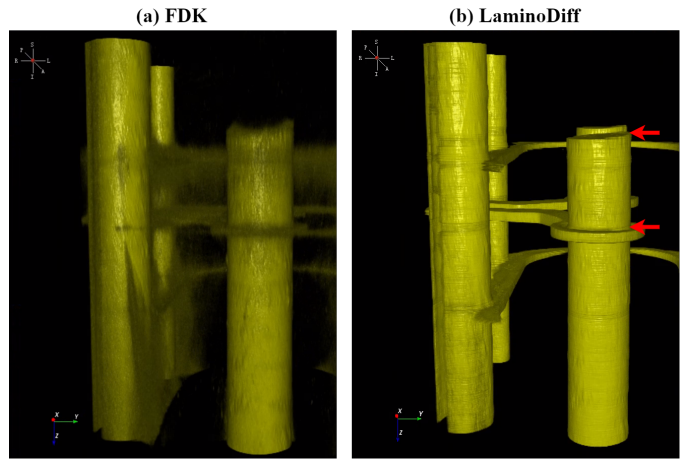


Fig. 12. 3D rendering and dimensional quantification of a Stub structure in a high-frequency PCB. (a) The FDK reconstruction. (b) The proposed LaminoDiff reconstruction. The red arrows indicate the precise start (top) and end (bottom) planes identified for the stub length measurement.

tural layout. The cylindrical geometry of the vias and the planar surfaces of the stub are rendered with high fidelity, significantly mitigating the uncertainty in boundary delineation. As indicated by the red arrows, the critical geometric features—specifically the potential z -start and z -end reference planes—are clearly restored and distinguishable from the background. This structural clarity provides a robust geometric basis for downstream metrology algorithms. The restoration of these features boundaries demonstrates that LaminoDiff effectively bridges the gap between rough visual inspection and precision metrology, unlocking the potential for automated quantitative analysis that was previously unattainable with conventional reconstruction algorithms.

E. Ablation Study

Finally, to investigate the optimal strategy for prior generation, we conducted an ablation study focusing on the impact of the source domain distribution. As visualized in Fig. 13, we compared our proposed fusion prior against direct numerical guidance and style-transfer approaches.

Counter-intuitively, the experiment utilizing the ideal numerical phantom directly as a prior presented in Fig. 13 (c) yielded the poorest performance, exhibiting severe contrast degradation and feature washout. While the numerical phantom represents the geometric ground truth, its pixel intensity distribution differs fundamentally from the continuous, physics-based attenuation coefficients found in X-ray imaging. This creates a domain gap. Since the diffusion model was trained on data adhering to X-ray physical degradation features, it failed to generalize to this perfect out-of-distribution input, resulting in an inference collapse. Alternative strategies using CycleGAN to bridge this gap, as illustrated in Fig. 13 (d) and (e), also showed distinct limitations. While these methods attempted to remap the phantom to a realistic CT or CL style, they introduced stochastic errors. For instance, the pseudo-CT prior shown in Fig. 13 (d) generated high-contrast features but suffered from halo artifacts and hallucinated edges, which

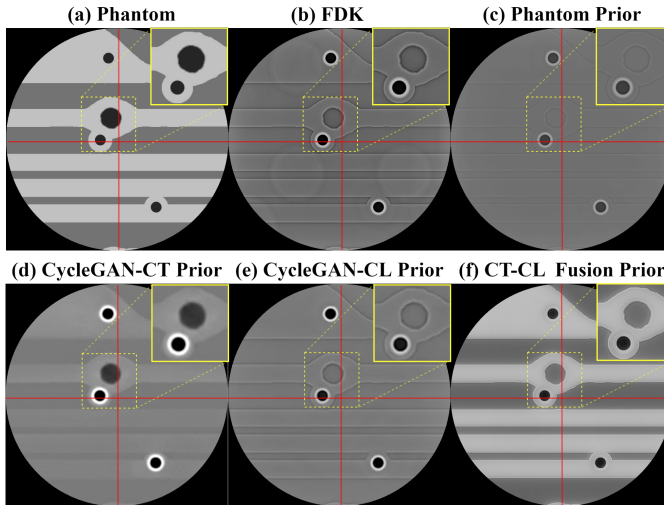


Fig. 13. Visual comparison of ablation studies on different prior guidance strategies. (a) The noise-free numerical phantom. (b) The artifact-corrupted FDK reconstruction. (c)-(f) Reconstruction results generated by the diffusion model conditioned on different priors: (c) conditioned on CycleGAN-translated CT-style images; (d) conditioned on CycleGAN-translated CL-style images; (e) conditioned directly on the ideal numerical phantom; and (f) conditioned on our proposed CT-CL fusion prior. All images are displayed with an intensity range of [25.5, 284.5].

were propagated into the final reconstruction. In stark contrast, our proposed method displayed in Fig. 13 (f), utilizing the CT-CL fusion prior, achieved superior reconstruction quality. By fusing the spectral information in the latent space, our prior inherently preserves the correct physical intensity statistics while maintaining the structural integrity of the phantom. This allows the network to focus on artifact removal without being hindered by domain shifts or hallucinated noise, confirming that physical consistency in the guidance signal is as critical as geometric accuracy.

V. CONCLUSION

In this work, a generative framework, LamoDiff, is designed to mitigate the severe aliasing artifacts inherent in CL. By reformulating the reconstruction task as a conditional generative process, our method effectively mitigates the dependence on paired real data, which represents a bottleneck that often restricts supervised deep learning applications in physical NDT. The core innovation lies in a latent spatial fusion strategy that decouples geometric consistency from artifact reduction, ensuring robust structure recovery even under severe limited-angle conditions. Extensive experiments on simulated datasets and real-world industrial PCB samples demonstrate that LamoDiff achieves competitive performance compared to existing data-driven approaches. By significantly reducing aliasing artifacts and enhancing edge definition, the proposed method establishes a robust geometric foundation for quantitative assessment of internal microstructures. These improvements suggest promising potential for reliable defect characterization in industrial inspection scenarios. While the proposed LamoDiff framework achieves significant improvements in artifact removal and in-plane structure recovery, residual anisotropy remains in the reconstruction quality along

the scan axis compared to high-fidelity in-plane results. The inherent missing cone problem remains a major challenge in acquiring high-frequency spectral information in the vertical direction and can lead to interlayer discontinuities. To bridge the gap between the lateral and longitudinal directions, we plan to introduce pseudo-3D spatial constraints or interlayer attention mechanisms, aiming to establish correlations between adjacent layers, suppress longitudinal blurring, and achieve isotropic 3D imaging resolution.

REFERENCES

- [1] J. Zhou, M. Maisl, H. Reiter, and W. Arnold, “Computed laminography for materials testing,” *Applied Physics Letters*, vol. 68, no. 24, pp. 3500–3502, 1996.
- [2] P. Aryan, S. Sampath, and H. Sohn, “An overview of non-destructive testing methods for integrated circuit packaging inspection,” *Sensors*, vol. 18, no. 7, p. 1981, 2018.
- [3] Y. Cai, P. Li, J. Wang *et al.*, “Recent advances in computed laminography for nondestructive testing of plate-shell objects,” *Chinese Journal of Scientific Instrument*, vol. 41, no. 1, pp. 11–25, 2020.
- [4] W. Du, F. Iacoviello, M. Mirza, S. Zhou, J. Bu, S. Feng, P. S. Grant, R. Jervis, D. J. Brett, and P. R. Shearing, “X-ray computed laminography: A brief review of mechanisms, reconstruction, applications and perspectives,” *Materials Today*, 2025.
- [5] A. C. Kak and M. Slaney, *Principles of Computerized Tomographic Imaging*. SIAM, 2001.
- [6] H. K. Tuy, “An inversion formula for cone-beam reconstruction,” *SIAM Journal on Applied Mathematics*, vol. 43, no. 3, pp. 546–552, 1983.
- [7] B. D. Smith, “Image reconstruction from cone-beam projections: Necessary and sufficient conditions and reconstruction methods,” *IEEE Transactions on Medical Imaging*, vol. 4, no. 1, pp. 14–25, 2007.
- [8] L. A. Feldkamp, L. C. Davis, and J. W. Kress, “Practical cone-beam algorithm,” *Journal of the Optical Society of America A*, vol. 1, no. 6, pp. 612–619, 1984.
- [9] T. Jia, S. Liu, X. Sun, C. Wei, Z. Qiao, and B. Liu, “GPU implementation of CL iterative reconstruction algorithm,” *Chinese Journal of Stereology and Image Analysis*, vol. 25, no. 4, pp. 393–400, 2020.
- [10] J. Pengxiang, H. Xiaodong, and Z. Jing, “Study on the Fourier defects of cone-beam computed laminography,” *IEEE Access*, 2025.
- [11] J. Wang, Y. Zou, Q. Qin, Z. Liu, and Y. Chen, “Truncated projection CL reconstruction based on TS-FBP,” *Optics Express*, vol. 33, no. 12, pp. 25 415–25 435, 2025.
- [12] Y. Zhao, J. Xu, H. Li, and P. Zhang, “Edge information diffusion-based reconstruction for cone beam computed laminography,” *IEEE Transactions on Image Processing*, vol. 27, no. 9, pp. 4663–4675, 2018.
- [13] R. Zhao, X. Hu, Y. Jiang, M. Chen, and J. Zou, “Iterative difference deblurring algorithm for linear computed laminography,” *Optics Express*, vol. 29, no. 19, pp. 30 123–30 139, 2021.
- [14] L. Sun, G. Zhou, Z. Qin, S. Yuan, Q. Lin, Z. Gui, and M. Yang, “A reconstruction method for cone-beam computed laminography based on projection transformation,” *Measurement Science and Technology*, vol. 32, no. 4, p. 045403, 2021.
- [15] H. Qi, Z. Chen, J. Guo, and L. Zhou, “Sparse-view computed tomography image reconstruction via a combination of L1 and SL0 regularization,” *Bio-Medical Materials and Engineering*, vol. 26, no. 1_suppl, pp. S1389–S1398, 2015.
- [16] J. Lu, Y. Liu, P. Zhang, Z. Li, M. Yang, and Z. Gui, “An anisotropic alternating regularization-based reconstruction algorithm for cone beam computed laminography,” *NDT & E International*, vol. 138, p. 102898, 2023.
- [17] J. Lu, Y. Liu, Y. Chen, H. Shu, Z. Li, J. Kang, and Z. Gui, “Cone beam computed laminography based on adaptive-weighted dynamic-adjusted relative total variation,” *Nuclear Instruments and Methods in Physics Research Section A: Accelerators, Spectrometers, Detectors and Associated Equipment*, vol. 1051, p. 168200, 2023.
- [18] Y. Xi, Z. Qiao, A. Wang, C. Fang, and F. Liu, “Pig-DTpV: A prior information guided directional TpV algorithm for orthogonal translation computed laminography,” *Displays*, vol. 84, p. 102812, 2024.
- [19] C. Tan, G. Zhong, X. Lin, Q. Li, H. Zou, and L. Duan, “Orthogonal translation computed laminography aliasing artifacts elimination via adaptive L0 gradient minimization,” in *2024 Academic Conference of China Instrument and Control Society (ACCIS)*. IEEE, 2024, pp. 185–190.

[20] Y. Liu, H. Shu, Y. Liu, P. Zhang, L. Wang, P. Haigron, and Z. Gui, “3-D computed laminography based on a sequential regularization,” *IEEE Transactions on Nuclear Science*, 2025.

[21] C. Wang, Y. He, J. Wang, and W. Yu, “A conjugate gradient weighted least squares reconstruction method with region of interest correction for cone-beam rotational computed laminography,” *NDT & E International*, vol. 155, p. 103396, 2025.

[22] T. Jia, C. Wei, M. Zhu, R. Shi, Z. Wang, X. Cui, and B. Liu, “The multi-scale fusion reconstruction algorithm of CT and CL,” *Physica Scripta*, vol. 98, no. 10, p. 105114, 2023.

[23] M. Zuber, M. Laaß, E. Hamann, S. Kretschmer, N. Hauschke, T. van de Kamp, T. Baumbach, and T. Koenig, “Augmented laminography, a correlative 3D imaging method for revealing the inner structure of compressed fossils,” *Scientific Reports*, vol. 7, no. 1, p. 41413, 2017.

[24] P. Ji, Y. Jiang, R. Zhao, and J. Zou, “Fusional laminography: A strategy for exact reconstruction on CL and CT information complementation,” *NDT & E International*, vol. 141, p. 102991, 2024.

[25] Z. Gui, Y. Liu, Y. Liu, W. Liu, R. Yan, L. Wang, P. Zhang, Q. Zhang, and H. Shu, “3-D computed laminography based on prior images and total variation,” *IEEE Transactions on Nuclear Science*, vol. 70, no. 3, pp. 189–199, 2023.

[26] K. H. Jin, M. T. McCann, E. Froustey, and M. Unser, “Deep convolutional neural network for inverse problems in imaging,” *IEEE Transactions on Image Processing*, vol. 26, no. 9, pp. 4509–4522, 2017.

[27] H. Chen, Y. Zhang, M. K. Kalra, F. Lin, Y. Chen, P. Liao, J. Zhou, and G. Wang, “Low-dose CT with a residual encoder-decoder convolutional neural network,” *IEEE Transactions on Medical Imaging*, vol. 36, no. 12, pp. 2524–2535, 2017.

[28] T. Jia, L. Shi, C. Wei, R. Shi, and B. Liu, “Correction of motion artifact in CL based on MAFusNet,” *Journal of X-Ray Science and Technology*, vol. 31, no. 2, pp. 393–407, 2023.

[29] O. Ronneberger, P. Fischer, and T. Brox, “U-Net: Convolutional networks for biomedical image segmentation,” in *International Conference on Medical Image Computing and Computer-Assisted Intervention*. Springer, 2015, pp. 234–241.

[30] L. Shi, C. Wei, T. Jia, and B. Liu, “An automatic measurement method of PCB stub based on rotational computed laminography imaging,” *IEEE Transactions on Nuclear Science*, vol. 70, no. 9, pp. 2201–2211, 2023.

[31] L. Shi, C. Wei, T. Jia, Y. Zhao, and B. Liu, “A PCB image segmentation model based on rotational x-ray computed laminography imaging,” *Journal of X-Ray Science and Technology*, vol. 32, no. 4, pp. 1079–1098, 2024.

[32] X. Zou, W. Shi, M. Du, and Y. Xing, “Artifact reduction in rotational computed laminography using a deep learning method,” *Optics and Lasers in Engineering*, vol. 187, p. 108881, 2025.

[33] Y. Feng, J. Liu, Y. Ji, and S. Luo, “Multi-scale image artifacts removal network for reducing limited-angle artifacts of CL system,” *Sensing and Imaging*, vol. 26, no. 1, p. 71, 2025.

[34] J.-Y. Zhu, T. Park, P. Isola, and A. A. Efros, “Unpaired image-to-image translation using cycle-consistent adversarial networks,” in *Proceedings of the IEEE International Conference on Computer Vision*, 2017, pp. 2223–2232.

[35] Y. Zhang, S. Miao, T. Mansi, and R. Liao, “Task driven generative modeling for unsupervised domain adaptation: Application to x-ray image segmentation,” in *International Conference on Medical Image Computing and Computer-Assisted Intervention*. Springer, 2018, pp. 599–607.

[36] Y. Song and S. Ermon, “Generative modeling by estimating gradients of the data distribution,” *Advances in Neural Information Processing Systems*, vol. 32, 2019.

[37] J. Ho, A. Jain, and P. Abbeel, “Denoising diffusion probabilistic models,” *Advances in Neural Information Processing Systems*, vol. 33, pp. 6840–6851, 2020.

[38] J. Song, C. Meng, and S. Ermon, “Denoising diffusion implicit models,” *arXiv preprint arXiv:2010.02502*, 2020.

[39] J. Liu, R. Anirudh, J. J. Thiagarajan, S. He, K. A. Mohan, U. S. Kamilov, and H. Kim, “Dolce: A model-based probabilistic diffusion framework for limited-angle ct reconstruction,” in *Proceedings of the IEEE/CVF international conference on computer vision*, 2023, pp. 10498–10508.

[40] Y. Liu, Y. Wen, Z. Zhou, J. Ma, L. Wang, Y. Yao, L. Shi, and Q. Liu, “PWD: Prior-guided and wavelet-enhanced diffusion model for limited-angle CT,” *arXiv preprint arXiv:2507.05317*, 2025.

[41] J. Ho and T. Salimans, “Classifier-free diffusion guidance,” *arXiv preprint arXiv:2207.12598*, 2022.

[42] C. Zhang, S. Bengio, M. Hardt, B. Recht, and O. Vinyals, “Understanding deep learning requires rethinking generalization,” in *International Conference on Learning Representations*, 2017.

[43] D. Arpit, S. Jastrzebski, N. Ballas, D. Krueger, E. Bengio, M. S. Kanwal, T. Maharaj, A. Fischer, A. Courville, Y. Bengio *et al.*, “A closer look at memorization in deep networks,” in *International conference on machine learning*. PMLR, 2017, pp. 233–242.

[44] M. Mohri, A. Rostamizadeh, and A. Talwalkar, *Foundations of machine learning*. MIT press, 2018.

[45] J. Lehtinen, J. Munkberg, J. Hasselgren, S. Laine, T. Karras, M. Aittala, and T. Aila, “Noise2noise: Learning image restoration without clean data,” in *International Conference on Machine Learning*. International Machine Learning Society, 2018, pp. 4620–4631.

[46] Z. Wang, A. C. Bovik, H. R. Sheikh, and E. P. Simoncelli, “Image quality assessment: From error visibility to structural similarity,” *IEEE Transactions on Image Processing*, vol. 13, no. 4, pp. 600–612, 2004.

[47] N. Otsu *et al.*, “A threshold selection method from gray-level histograms,” *Automatica*, vol. 11, no. 285-296, pp. 23–27, 1975.